

## Article

# Fabricated High-Strength, Low-Elastic Modulus Biomedical Ti-24Nb-4Zr-8Sn Alloy via Powder Metallurgy

Amy X. Y. Guo <sup>1</sup>, Bin Cao <sup>1</sup> , Zihan Wang <sup>1</sup>, Xiao Ma <sup>2,\*</sup> and Shan Cecilia Cao <sup>1,\*</sup>

<sup>1</sup> Materials Genome Institute, Shanghai University, Shanghai 200444, China; guoxiaoyun@shu.edu.cn (A.X.Y.G.); bcao@shu.edu.cn (B.C.)

<sup>2</sup> Institute for the Conservation of Cultural Heritage, Shanghai University, Shanghai 200444, China

\* Correspondence: maxiao@shu.edu.cn (X.M.); scao@shu.edu.cn (S.C.C.)

**Abstract:** With the huge demands of an aging society, it is urgent to develop a new generation of non-toxic titanium alloy to match the modulus of human bone. Here, we prepared bulk Ti2448 alloys by powder metallurgy technology, and focused on the influence of the sintering process on the porosity, phase composition, and mechanical properties of the initial sintered samples. Furthermore, we performed solution treatment on the samples under different sintering parameters to further adjust the microstructure and phase composition, so as to achieve strength enhancement and reduction of Young's modulus. Solution treatment can effectively inhibit the continuous  $\alpha$  phase precipitated along the grain boundaries of the  $\beta$  matrix, which is beneficial to the fracture resistance. Therefore, the water-quenched sample exhibits good mechanical properties due to the absence of acicular  $\alpha$ -phase. Samples sintered at 1400 °C and subsequently water quenched have excellent comprehensive mechanical properties, which benefit from high porosity and the smaller feature size of microstructure. To be specific, the compressive yield stress is 1100 MPa, the strain at fracture is 17.5%, and the Young's modulus is 44 GPa, which are more applicable to orthopedic implants. Finally, the relatively mature sintering and solution treatment process parameters were screened out for reference in actual production.

**Keywords:** Ti2448 alloy; microstructure analysis; porosity; mechanical properties



**Citation:** Guo, A.X.Y.; Cao, B.; Wang, Z.; Ma, X.; Cao, S.C. Fabricated High-Strength, Low-Elastic Modulus Biomedical Ti-24Nb-4Zr-8Sn Alloy via Powder Metallurgy. *Materials* **2023**, *16*, 3845. <https://doi.org/10.3390/ma16103845>

Academic Editor: Jarosław Jakubowicz

Received: 31 March 2023

Revised: 5 May 2023

Accepted: 14 May 2023

Published: 19 May 2023



**Copyright:** © 2023 by the authors. Licensee MDPI, Basel, Switzerland. This article is an open access article distributed under the terms and conditions of the Creative Commons Attribution (CC BY) license (<https://creativecommons.org/licenses/by/4.0/>).

## 1. Introduction

Titanium alloy is widely used as implant material because of its high specific strength, low elastic modulus, good corrosion resistance, and excellent biocompatibility, and titanium alloy has become an important biomedical material [1–4]. Ti-6Al-4V is the most widely used titanium alloy in clinical medicine that has been thoroughly studied, including manufacturing techniques, microstructure characterization, mechanical performance, and corrosion resistance [5–7]. However, there is still an urgent need to further develop new type titanium alloys. First, the elastic modulus of titanium alloy implants (~110 GPa) is much higher than that of human bone (12–30 GPa) [8,9]. Orthopedic implants with incompatible elastic modulus could generate stress shielding after implantation, leading to loosening or fracture of the implant in the human body [10,11]. Second, alloying elements such as Ni, Al, and V are toxic and allergenic, and they may result in Alzheimer's and neurological diseases when they are released into the human body through corrosion [12,13].

In order to overcome the above problems, a new generation of non-toxic medical titanium alloys with lower modulus and better biocompatibility have been developed in recent years [14,15]. Bordbar-Khiabani et al. [16] developed Ti-Nb-Zr-Si alloy, which exhibit superior corrosion resistance and favorable cell-materials interactions in vitro. Hao et al. devised the Ti-24Nb-4Zr-8Sn (wt.%) alloy, which is known as the representative of the next generation of medical materials because of its excellent mechanical properties and biocompatibility [17,18]. First of all, polycrystalline Ti2448 has high strength (~1150 MPa), low

elastic modulus (~56 GPa), large recoverable strain (~3.3%), and a weak grain refinement strengthening effect [17]. Especially the <100> oriented single crystal exhibits weak non-linear elasticity with large elastic strain (~2.5%) and low Young's modulus (27.1 GPa) [19]. Moreover, Ti2448 alloy does not contain Al and V elements, which are toxic to the human body. Nune et al. reported that the alloy formed fine apatite-like crystals in simulated body fluids, which confirmed the excellent biological activity of the alloy [20]. Obbard et al. [21] found that oxygen reduces the non-line recoverable strain, shortens the stress plateau and obscures the double yield points of forged Ti2448 alloy. Li et al. [21] investigated the tensile deformation mechanism of a high-oxygen Ti2448 alloy fabricated by powder metallurgy, and they pointed out that both dislocation slide and stress-induced phase transformation contribute to the plastic deformation of the alloy. Tang et al. [22] designed experiments to explore the role of 3D printed Ti2448 in macrophage activation and related osteogenesis and angiogenesis. More research focused on the biocompatibility of Ti2448 alloys prepared by powder metallurgy [23–25].

Furthermore, research of the ball milling procedure has greatly promoted the development of Ti-based powder metallurgy technology [26,27]. Yim et al. [28] found that mechanical stimulation was able to suppress the smoke of gas-atomized Ti-48Al-2Cr-2Nb powder using Al<sub>2</sub>O<sub>3</sub> and WC ball milling. Salur et al. [29] studied the effect of ball milling time on the structural characteristics and mechanical properties of the nano-sized Y<sub>2</sub>O<sub>3</sub> particle, which reinforced aluminum matrix composites produced by the powder metallurgy route. Pradeep et al. [30] synthesized the Ti-Mg-Sr alloy powder by process of mechanical alloying, and the grain size of the Ti-Mg-Sr particles decreased to a nanoscale regime from a micron scale. The developed novel Ti-Mg-Sr alloy could be useful for biomedical application.

However, optimizing the preparation protocol to meet the needs of the medical implant market is far-reaching and critical. Common methods include powder metallurgy [31], electron beam melting [2], and selective laser melting [32]. Among them, although powder metallurgy is relatively traditional, it has economic advantages. As a near-net shape technology, it can reduce machining processes and improve the production efficiency of structural parts [33]. The application of powder metallurgy technology can further popularize the practical application fields of titanium alloy materials, especially in civil fields [34]. Here we prepared bulk Ti2448 alloys by powder metallurgy technology, and focused on the influence of the sintering process on the porosity, phase composition, and mechanical properties of the initial sintered state. Furthermore, we performed solution treatment on the samples under different sintering parameters to further tuning of the microstructure and phase composition, so as to achieve strength enhancement and reduction of Young's modulus. Finally, the relatively mature sintering and solution treatment process parameters were screened out to promote the wide application of Ti2448 in medical implants.

## 2. Methods and Materials

### 2.1. Materials and Processing

A schematic representation of the main stages of experimental work performed in the present study are shown in Figure 1. Ti2448 alloy was manufactured by using elemental powders, which are more flexible and for which it is easier to adjust the composition. High-purity Ti, Nb, Zr, and Sn powders as raw material, and we mixed the powders at a mass ratio of 64:24:4:8 and then put them into a ball miller (QM-3SP4, Changsha Miqi Instrument Equipment Co., Ltd., Changsha, China) to achieve mechanical alloying. We adopted ethanol as a process control agent (PCA) to avoid cold welding and bonding between the powder particles and the balls as well as the agglomeration of the powder during milling. The grinding had a speed of 300 rpm and lasted for 20 h. After ball milling, the slurry was dried at 60 °C for 10 h under vacuum, and the powder and grinding balls were separated using a 300-mesh sieve to obtain pre-alloyed powder. Subsequent cold pressing (YLJ-CSP-15, MTI Corporation, Hefei, China) was used to fabricate green compacts (Φ10 mm × 15 mm).



**Figure 1.** A schematic representation of the main stages of experimental work performed in the present study: (A) mechanical alloying procedure; (B) powder metallurgy procedure; (C) equipment used for microstructure and mechanical properties characterization.

The green compacts were sintered in a  $\text{Al}_2\text{O}_3$  tube furnace under a flowing Ar atmosphere, during which the samples were sintered at different temperatures (1400 °C, 1450 °C and 1500 °C) for 12 h and then cooled down to room temperature with the furnace. The as-sintered samples were solution-treated at 1000 °C for 1 h and subsequently water quenched.

## 2.2. Microstructure Characterization

The X ray diffraction (XRD) measurements were carried out with a Bruker D8 advance (D8, Bruker, Germany), with a Cu target operating at the anode target voltage of 40 kV, where the target current is 30 mA, the scanning speed is  $0.01^\circ/\text{s}$ , the integration time of one step is 2 s, and the scanning angle is  $30^\circ\sim 90^\circ$ . Whole Pattern fitting of powder X-ray diffraction was by Expectation Maximum (WPEM) software (WPEM, Beta version). The primary goal of WPEM is to develop an open-source diffraction whole pattern fitting software that offers high solution efficiency and precision. WPEM also provide the open-source address ([github.com](https://github.com), accessed on 30 March 2023/Bin-Cao/WPEM), allowing researchers and scientists to access and utilize this powerful software for their structural analysis needs. The WPEM analyzes a whole XRD patten with the Bragg law-based XRD theory and the Expectation-Maximum algorithm. The software is particularly effective in determining complex crystal structures and decoupling heavily overlapped Bragg peaks in the whole XRD pattern.

The microstructure and component distribution were characterized by the scanning electron microscopy (SEM, Sigma 500, Carl Zeiss, Jena, Germany) with an operating voltage of 15 kV and a working distance of 8.0 mm. The samples for microstructure observation were grinded and polished, and were then etched using a mixed solution of HF, HNO<sub>3</sub>, and H<sub>2</sub>O with a volume ratio of 1:3:7. The compositions were assessed by energy dispersive spectroscopy (EDS, AZTEC, Oxford Instrument, Abingdon, UK) analysis.

### 2.3. Mechanical Testing

Specimens for compressive tests were cut from the rods using an electro-discharge machine. The compressive tests were conducted at room temperature using a universal testing machine (Material Testing System Model 810, Eden Prairie, MN, USA) equipped with an extensometer and the strain rate was set at  $1.0 \times 10^{-3} \text{ s}^{-1}$ . The mechanical response under the compressive load condition was investigated by plotting the load vs. displacement curve until the samples get fractured. The Young's modulus was determined from the slope of the stress vs. strain curve for each sample.

## 3. Results and Discussion

### 3.1. Powder Size and Microstructure Characterization

The SEM images of the raw powders are shown in Figure 2. It can be obtained from the statistical results of multiple images that the non-spherical titanium powder has a diameter of 30  $\mu\text{m}$ , the non-spherical niobium powder has a diameter of 17  $\mu\text{m}$ , the non-spherical zirconium powder has a diameter of 10  $\mu\text{m}$ , the spherical tin powder has a diameter of 10  $\mu\text{m}$ . Their crystal structures correspond to hexagonal close packet (HCP), body centered cubic (BCC), HCP and tetragonal system, respectively. The Ti2448 powder after ball milling has a loose layered structure and has undergone mechanical alloying, as shown in Figure 3, with a diameter of about 15  $\mu\text{m}$  and composed of  $\alpha$  (HCP) and  $\beta$  (BCC) phases. This also shows that ball milling makes the elemental powder fully and uniformly mixed, which is helpful for the subsequent sintering process.

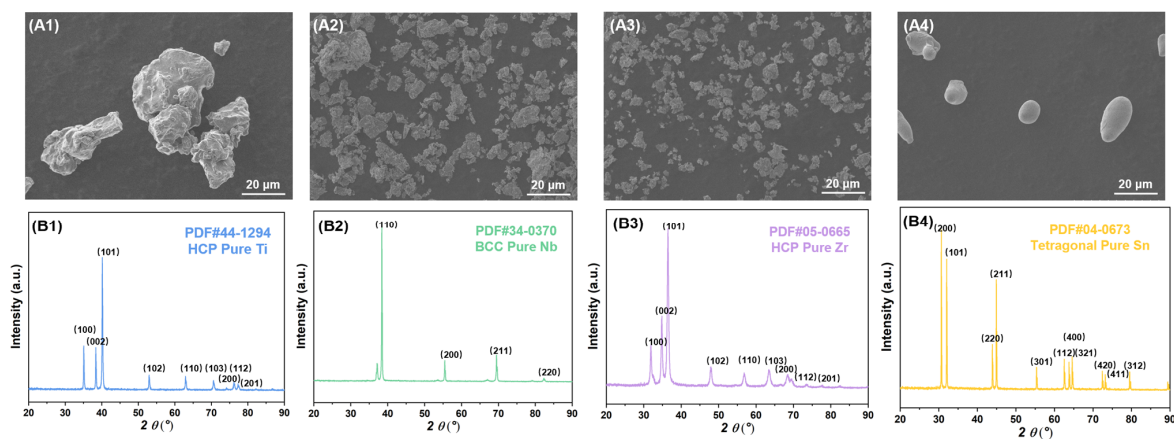
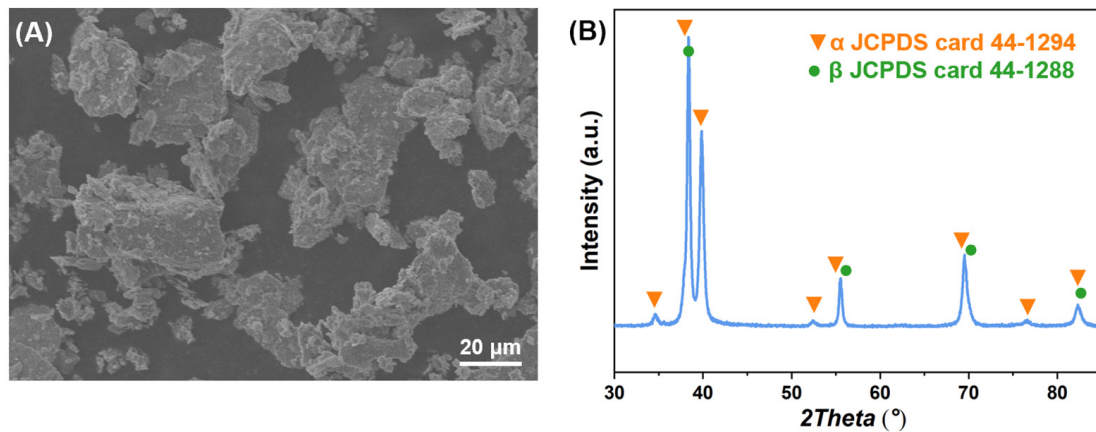


**Figure 2.** SEM images and XRD spectrums of raw powder: (A1,B1) titanium powder; (A2,B2) niobium powder; (A3,B3) zirconium powder; (A4,B4) tin powder.

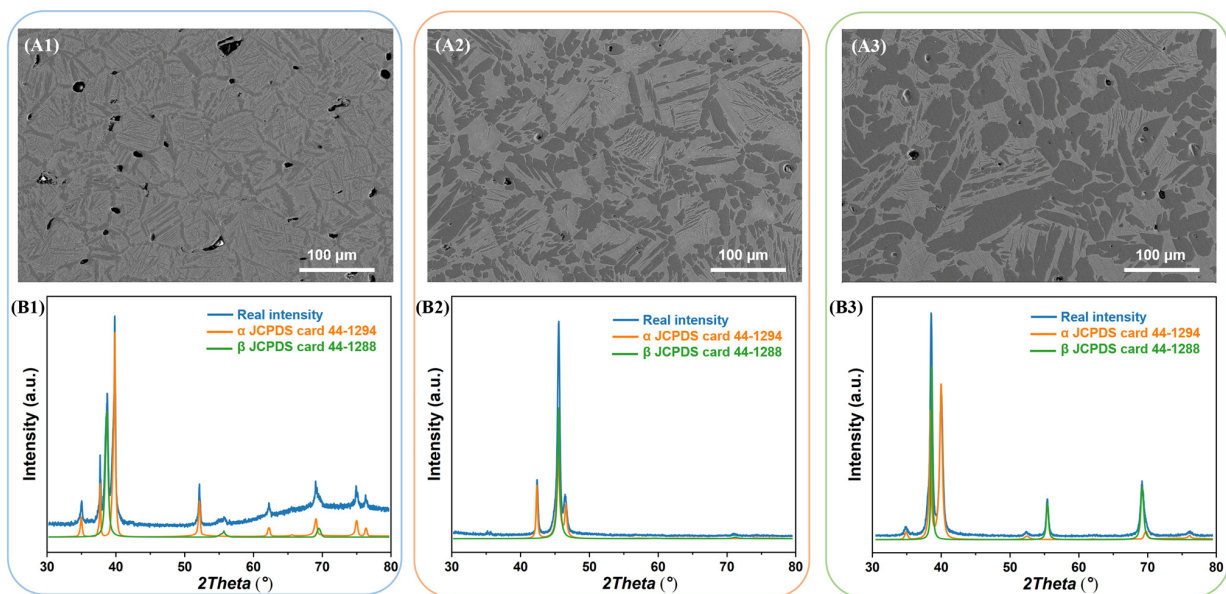
### 3.2. Microstructure Characterization of As-Sintered Samples

Figure 4 shows the microstructure and XRD patterns of the green samples, which are sintered at different temperatures, 1400  $^{\circ}\text{C}$ , 1450  $^{\circ}\text{C}$ , and 1500  $^{\circ}\text{C}$ , respectively. We abbreviate them as S1400, S1450, and S1500, respectively. First of all, the microstructure of the samples belong to the transformation  $\beta$  structure category, which is derived from sintering temperatures higher than the  $\beta$  transition temperature (850  $^{\circ}\text{C}$ ) [35] and the sintered samples cooled slowly with the furnace. The mixed structure formed by the decomposition of the  $\beta$  phase, and usually consisting of alternating lamellar  $\alpha$  and  $\beta$  arrange composition. The secondary  $\alpha$  phase inside the grains, though, while the continuous

$\alpha$  phase is precipitated along the grain boundaries of the  $\beta$  matrix, which is called the grain boundary  $\alpha$ -phase (GB- $\alpha$ ). The GB- $\alpha$  in titanium alloys is usually formed in conventionally manufactured titanium alloys due to the slow cooling process [36–39]. However, the characteristic size and porosity of the samples prepared under the three sintering processes are completely different, and the morphology and porosity are the key factors affecting the mechanical properties of the sintered samples.



**Figure 3.** (A) SEM images and (B) XRD spectrums of pre-alloyed powder.



**Figure 4.** SEM images and XRD spectrums of as-sintered samples: (A1,B1) S1400 sample; (A2,B2) S1450 sample; (A3,B3) S1500 sample.

The grain size of S1400 sample is about 60  $\mu\text{m}$ , the spherical  $\alpha$  phase is precipitated preferentially along the grain boundary, while the  $\alpha$  plates are precipitated inside the grain. Raising the sintering temperature can enhance the driving force of microstructure growth, which makes the grain size of S1450 and S1500 sample grow up to 80  $\mu\text{m}$  and 100  $\mu\text{m}$ , and the  $\alpha$  phase within the grain becomes coarse, correspondingly. With the elements partitioning during the sintering process, Nb and Zr are enriched in the  $\beta$  matrix and absent in the  $\alpha$  phase, and neutral elements Sn distribute uniformly in the whole region without recognizable segregation [40], as shown in Figure 5.

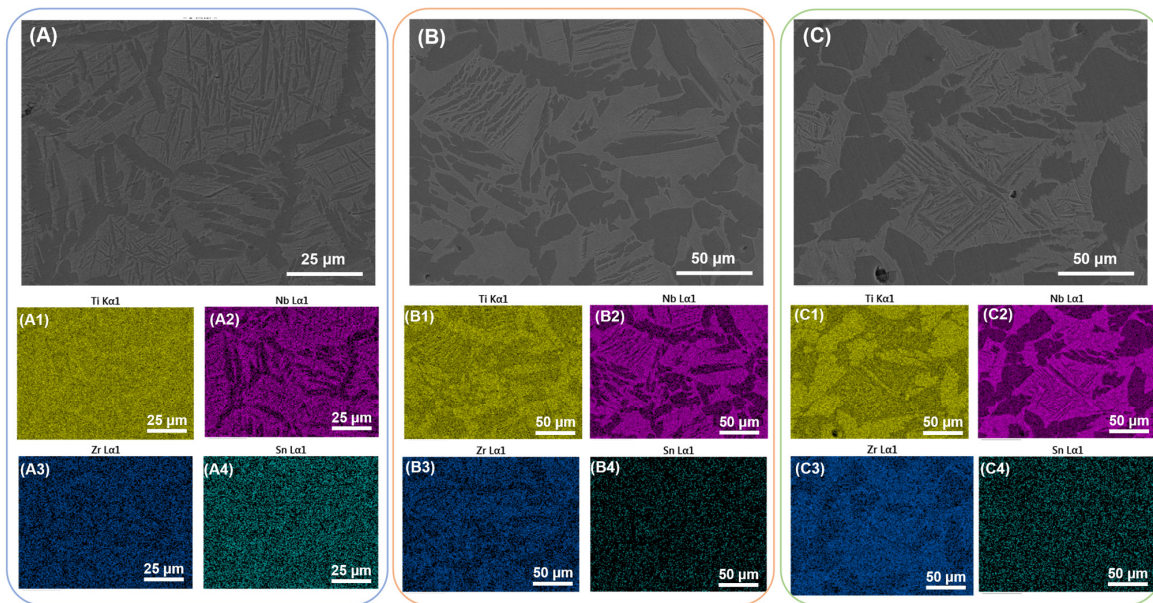


**Figure 5.** SEM images of the as-sintered samples and corresponding elemental maps: (A) and (A1–A4) S1400 sample; (B) and (B1–B4) S1450 sample; (C) and (C1–C4) S1500 sample.

### 3.3. Microstructure Characterization of Solution Treated Samples

In order to further optimize the microstructure, reduce the porosity, and improve the comprehensive mechanical properties, we performed solution treatment on the samples prepared by the three sintering processes, which are abbreviated as S1400 + Q, S1450 + Q and S1500 + Q, respectively. As shown in Figure 6, the microstructure of the S1400 + Q sample has changed significantly, the acicular  $\alpha$  phase inside the grain has disappeared, while the morphology of S1450 + Q and S1500 + Q was similar to that before the solution treatment. As shown in Figure 7, the results of EDS show that there is still obvious elemental separation in the sample. Based on the experimental results after solid solution treatment, water quenching did not achieve the ideal effect of inhibiting the  $\alpha$  phase, especially the S1450 + Q and S1500 + Q samples, which may be related to the loss of  $\beta$  stability elements at high temperature sintering [41].

We employed the expectation maximization (EM) algorithm Rietveld refinement to fit the XRD patterns in order to estimate the volume fraction of the  $\beta$  and  $\alpha$  phases. As shown in Figure 8, the  $\alpha$ -precipitated phase fractions of the samples sintered at 1400 °C, 1450 °C, and 1500 °C were 66.7%, 58.5%, and 60.7%, respectively, while the densities were 87%, 95%, and 92%, respectively. Solid solution treatment increased the density of the sample, resulting in densities of 90%, 98%, and 95% for S1400 + Q, S1450 + Q, and S1500 + Q, respectively. In contrast, solid solution treatment decreased the volume fraction of the  $\alpha$ -precipitated phase to 32.5%, 41.2%, and 46.9% for the same samples.

### 3.4. Mechanical Characterization and Fracture Analysis

To characterize the mechanical properties, we performed uniaxial compression tests on the samples with different preparation processes, as shown in Figure 9. The compressive yield strength, the Young's modulus, and the strain at fracture were extracted from the compressive stress-strain curves, and their values are shown in Figure 10. First of all, the sintering temperature has a significant influence on the mechanical properties of the specimen. The compressive yield strength of the S1400 sample is only 450 MPa, while the compressive yield strength of the S1450 and S1500 sample increases to 1250 MPa and 1450 MPa, respectively. On the contrary, the strain at fracture drops sharply with the elevation of the sintering temperature. The strain at fracture of the S1400 sample is 25%, while the strain at fracture of the S1450 and S1500 samples are only 3%. In addition, Young's modulus is very important for the effectiveness of implants in vivo, and we strive to obtain

samples with a modulus closer to that of human bone. As the sintering temperature elevates from 1400 °C to 1500 °C, the Young’s modulus rises from 62.5 GPa to 70.0 GPa. The presence of continuous GB- $\alpha$  may lead to a decrease in fracture-related performance, as it may obstruct the dislocation movement of adjacent  $\alpha$  colonies and  $\beta$  matrix [42,43]. Dislocations accumulate in continuous GB- $\alpha$ , resulting in strain localization, which, in turn, promotes crack initiation [44,45].

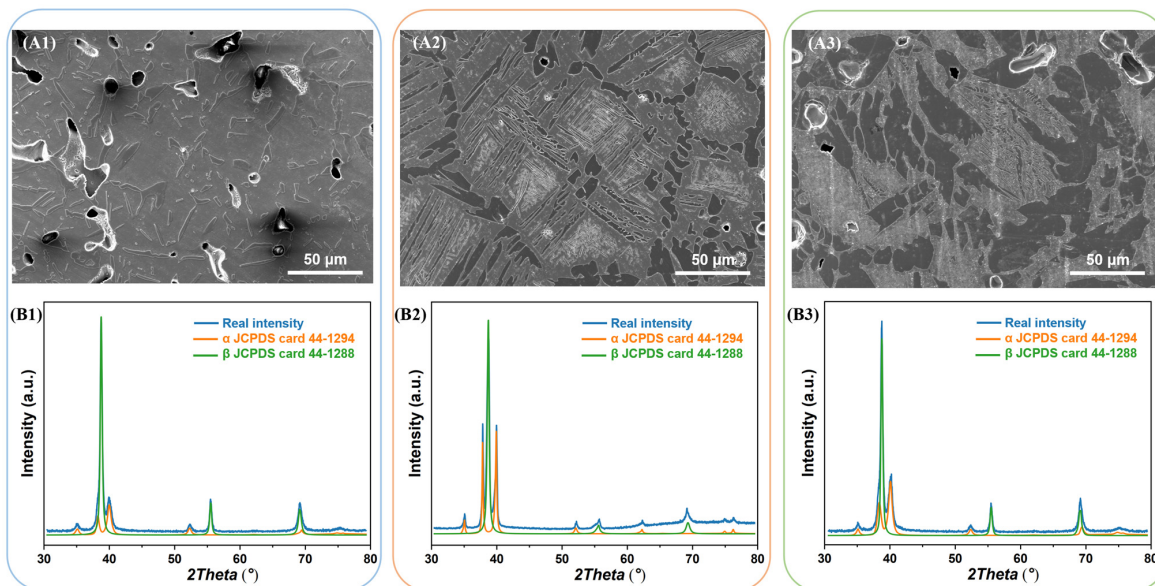


Figure 6. SEM images and XRD spectrums of the solution-treated samples: (A1,B1) S1400 + Q sample; (A2,B2) S1450 + Q sample; (A3,B3) S1500 + Q sample.

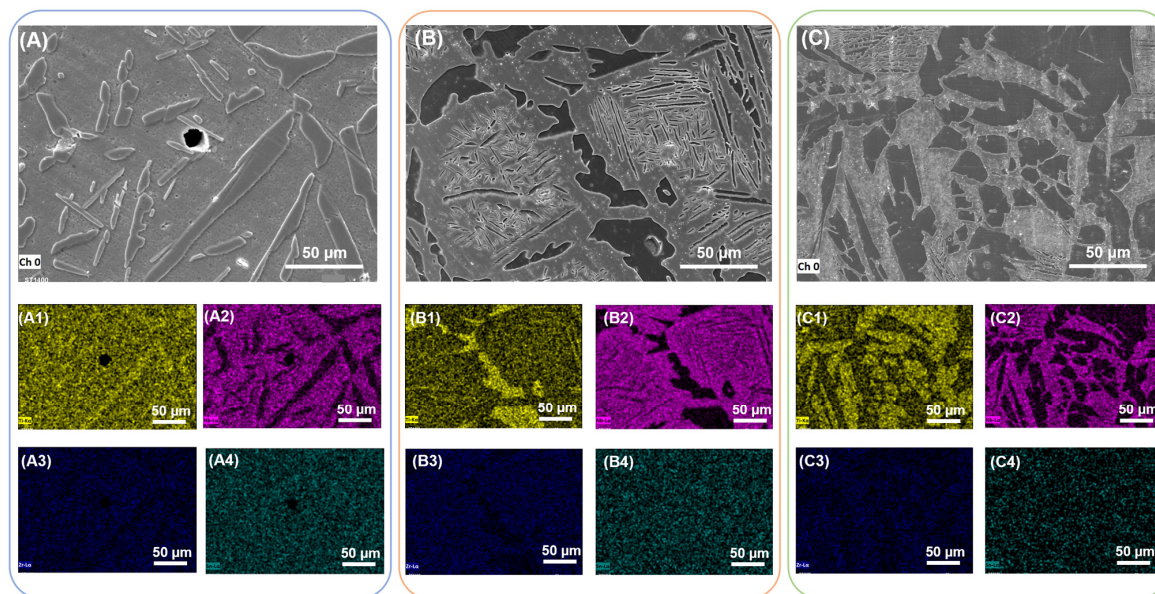
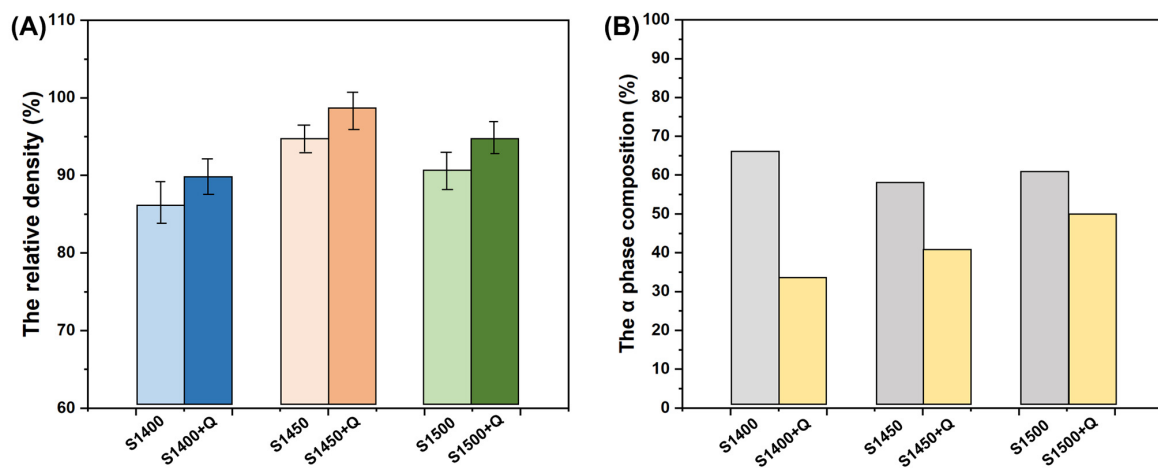
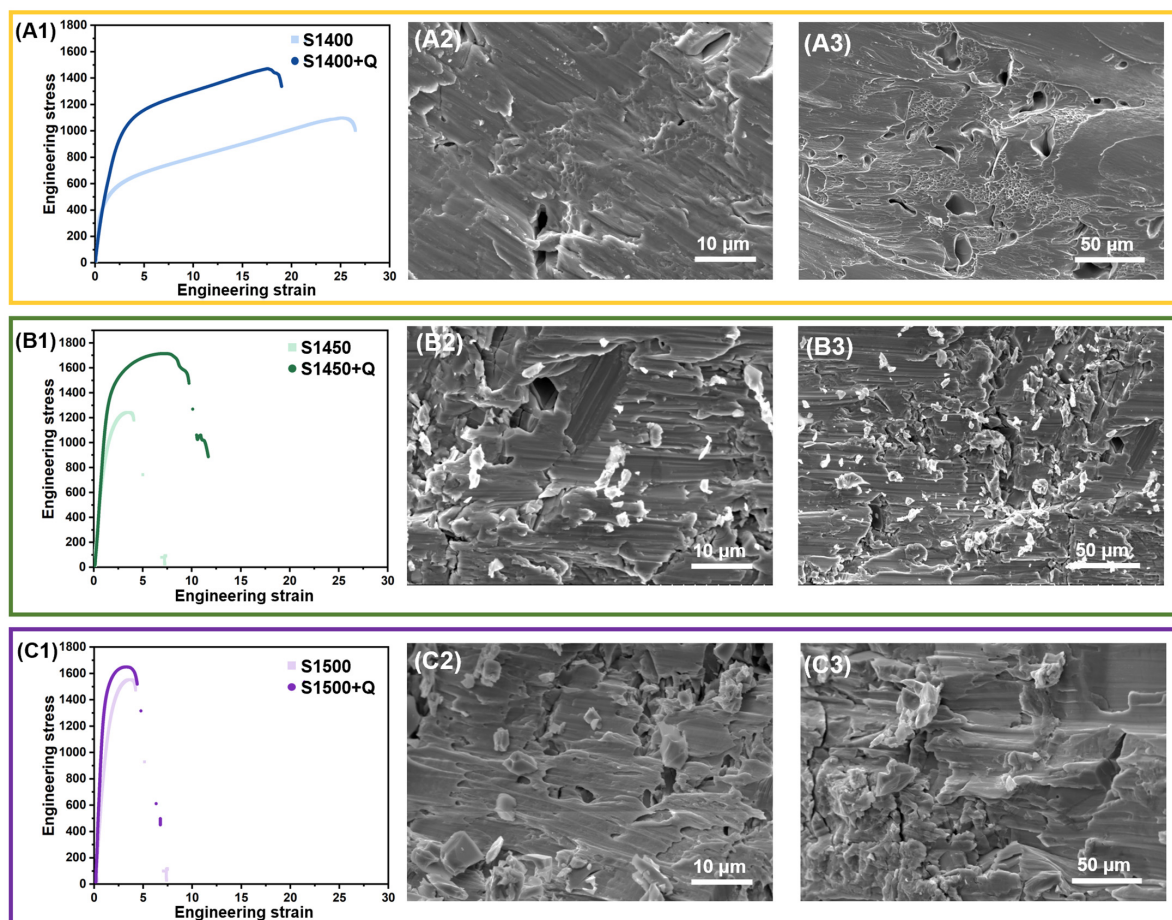


Figure 7. SEM images of the solution-treated samples and corresponding elemental maps: (A) and (A1–A4) S1400 + Q sample; (B) and (B1–B4) S1450 + Q sample; (C) and (C1–C4) S1500 + Q sample.



**Figure 8.** The relative density and phase composition of the as-sintered and water-quenched Ti2448 samples: (A) the relative density; (B) the  $\alpha$  phase composition.



**Figure 9.** The compressive stress-strain curves and fracture topography of the as-sintered and water-quenched Ti2448 samples: (A1) the compressive stress-strain curves of S1400 and S1400 + Q sample; (A2) fracture topography of S1400 sample; (A3) fracture topography of S1400 + Q sample; (B1) the compressive stress-strain curves of S1450 and S1450 + Q sample; (B2) fracture topography of S1450 sample; (B3) fracture topography of S1450 + Q sample; (C1) the compressive stress-strain curves of S1500 and S1500 + Q sample; (C2) fracture topography of S1500 sample; (C3) fracture topography of S1500 + Q sample.

Compared to the as-sintered samples, the solution treated samples exhibit much better mechanical properties, the compressive yield strength increased to 1100 MPa, 1550 MPa and 1650 MPa, respectively. The strain at fracture was relatively stable, dropped to 17.5% for the S1400 + Q sample, but slightly improved to 7.5% for the S1450 + Q sample, and was almost unchanged for the S1500 + Q sample. It benefitted from the substantial reduction of the  $\alpha$ -phase after quenching and the high porosity, and the Young's modulus of the S1400 + Q sample was further reduced to 44 GPa while the Young's modulus of the S1450 + Q and S1500 + Q samples increased slightly due to the improvement of density. Furthermore, the fracture surfaces of the S1400 + Q sample has abundant dimples, which imply good ductility of the materials. However, dimples disappeared in the other samples and were replaced by cleavage fractures along the lamellar  $\alpha$ -phase, as shown in Figure 9. The solution treatment can successfully suppress the precipitation of the  $\alpha$  phase in the Ti2448 alloy, yielding samples with a bulk  $\beta$  phase [31]. Liu et al. made a detailed investigation into the deformation behavior of GB- $\alpha$  with different morphologies, and they concluded that discontinuous GB- $\alpha$  is considered beneficial to the fracture resistance, since the dislocation motion is hypothesized to easily transfer through prior- $\beta$  grain boundaries at the sites without the GB- $\alpha$  [46,47]. Therefore, the water-quenched sample exhibits outstanding performance due to the absence of the acicular  $\alpha$ -phase. The S1400 + Q sample benefits from high porosity and a finer microstructure, and its comprehensive mechanical properties are more suitable for orthopedic implant application.

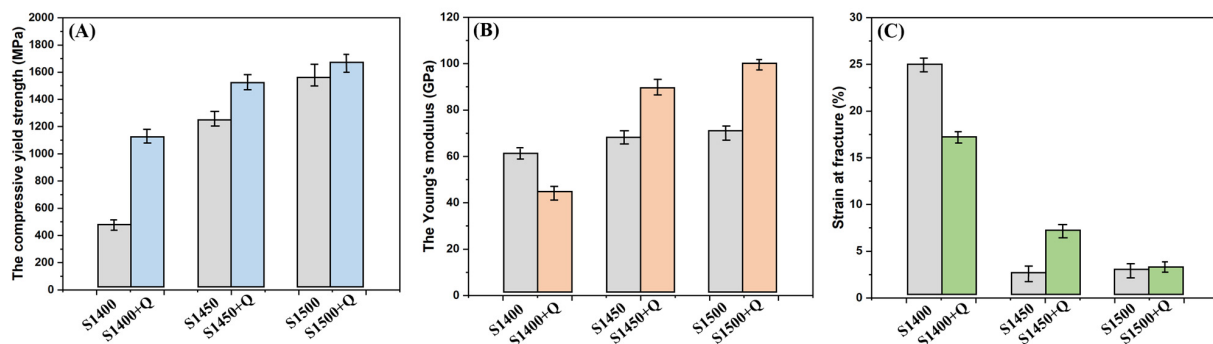


**Figure 10.** Mechanical properties of the as-sintered and water-quenched Ti2448 samples: (A) the compressive yield strength; (B) the Young's modulus; (C) strain at fracture.

#### 4. Conclusions

We used high-purity Ti, Nb, Zr, and Sn powders as raw materials and mixed the powders at a mass ratio of 64:24:4:8 to obtain pre-alloyed Ti2448 powder via ball milling. We focused on the influence of the sintering process on the porosity, phase composition, and mechanical properties of the initial sintered state. Furthermore, we performed solution treatment on the samples under different sintering parameters to further modify the microstructure and phase composition in order to achieve strength enhancement and a reduction of Young's modulus. Our work provides an economical and reliable process reference for promoting biomedical applications of Ti2448 alloys. The main conclusions are as follows:

- (1) The as-sintered samples have a two-phase microstructure where the secondary  $\alpha$  phase were inside the grains, while the primary  $\alpha$  phase precipitated along the grain boundaries of the matrix  $\beta$  phase. Beyond elements partitioning during the sintering process, Nb is enriched in the  $\beta$  matrix and absent in the  $\alpha$  phase.
- (2) The proportions of the  $\alpha$ -precipitated phases of the samples sintered at 1400 °C, 1450 °C, and 1500 °C were 66.7%, 58.5% and 60.7%, respectively, and the density was 87%, 95% and 92%, respectively.
- (3) The microstructure of S1400 + Q sample changed significantly, the acicular  $\alpha$  phase inside the grain disappeared, and the volume fraction of  $\beta$  phase was as high as 67.5%,

- while the morphology of S1450 + Q and S1500 + Q was similar to that before solution treatment, except that the porosity and the volume fraction of  $\alpha$  phase reduced slightly.
- (4) Solution treatment can effectively suppress the precipitation of  $\alpha$  phase in Ti2448 alloy, yielding samples with a bulk  $\beta$  phase. Therefore, the water-quenched sample exhibits good mechanical properties due to the absence of continuous GB- $\alpha$  phase. The S1400 + Q sample benefits from high porosity and a finer microstructure, and it has excellent comprehensive mechanical properties (the compressive yield stress is 1100 MPa, the strain at fracture is 17.5% and the Young's modulus is 44 GPa), which are more applicable to orthopedic implants.

**Author Contributions:** A.X.Y.G.: Investigation, Methodology, Writing—original draft, Writing—review and editing; B.C.: Data curation, Methodology, Software; Z.W.: Investigation, Funding acquisition; X.M.: Conceptualization, Visualization, Writing—review and editing; S.C.C.: Conceptualization, Project administration, Writing—review and editing. All authors have read and agreed to the published version of the manuscript.

**Funding:** The authors gratefully acknowledge financial support provided by the National Key Research and Development Program of China (Grant No. 2017YFB0701600) and Key Program of Science and Technology of Yunnan Province (Grant No. 202002AB080001-2).

**Institutional Review Board Statement:** Not applicable.

**Informed Consent Statement:** Not applicable.

**Data Availability Statement:** Not applicable.

**Acknowledgments:** The authors acknowledge the scientific suggestions and support from Tong-Yi Zhang.

**Conflicts of Interest:** The authors declare no conflict of interest.

## References

1. Dai, N.; Zhang, L.-C.; Zhang, J.; Chen, Q.; Wu, M. Corrosion behavior of selective laser melted Ti-6Al-4 V alloy in NaCl solution. *Corros. Sci.* **2016**, *102*, 484–489. [[CrossRef](#)]
2. Liu, Y.; Wang, H.; Li, S.; Wang, S.; Wang, W.; Hou, W.; Hao, Y.; Yang, R.; Zhang, L. Compressive and fatigue behavior of beta-type titanium porous structures fabricated by electron beam melting. *Acta Mater.* **2017**, *126*, 58–66. [[CrossRef](#)]
3. Li, J.; Bai, Y.; Fan, Z.; Li, S.; Hao, Y.; Yang, R.; Gao, Y. Effect of fluoride on the corrosion behavior of nanostructured Ti-24Nb-4Zr-8Sn alloy in acidulated artificial saliva. *J. Mater. Sci. Technol.* **2018**, *34*, 1660–1670. [[CrossRef](#)]
4. Li, H.F.; Qiu, K.J.; Zhou, F.Y.; Li, L.; Zheng, Y.F. Design and development of novel antibacterial Ti-Ni-Cu shape memory alloys for biomedical application. *Sci. Rep.* **2016**, *6*, 37475. [[CrossRef](#)] [[PubMed](#)]
5. Abd-elrhman, Y.; Gepreel, M.A.H.; Abdel-Moniem, A.; Kobayashi, S. Compatibility assessment of new V-free low-cost Ti-4.7Mo-4.5Fe alloy for some biomedical applications. *Mater. Des.* **2016**, *97*, 445–453. [[CrossRef](#)]
6. Mahlobo, M.G.R.; Chikosha, L.; Olubambi, P.A. Study of the corrosion properties of powder rolled Ti-6Al-4V alloy applied in the biomedical implants. *J. Mater. Res. Technol.* **2022**, *18*, 3631–3639. [[CrossRef](#)]
7. Buciumeanu, M.; Bagheri, A.; Shamsaei, N.; Thompson, S.; Silva, F.; Henriques, B. Tribocorrosion behavior of additive manufactured Ti-6Al-4V biomedical alloy. *Tribol. Int.* **2018**, *119*, 381–388. [[CrossRef](#)]
8. Hamidi, M.F.F.A.; Harun, W.S.W.; Samykano, M.; Ghani, S.A.C.; Ghazalli, Z.; Ahmad, F.; Sulong, A.B. A review of bio-compatible metal injection moulding process parameters for biomedical applications. *Mater. Sci. Eng. C* **2017**, *78*, 1263–1276. [[CrossRef](#)]
9. Li, S.; Xu, Q.; Wang, Z.; Hou, W.; Hao, Y.; Yang, R.; Murr, L. Influence of cell shape on mechanical properties of Ti-6Al-4V meshes fabricated by electron beam melting method. *Acta Biomater.* **2014**, *10*, 4537–4547. [[CrossRef](#)]
10. Heintz, P.; Müller, L.; Körner, C.; Singer, R.F.; Müller, F.A. Cellular Ti-6Al-4V structures with interconnected macro porosity for bone implants fabricated by selective electron beam melting. *Acta Biomater.* **2008**, *4*, 1536–1544. [[CrossRef](#)]
11. Afa, A.; Hassan, M.Z.; Ismail, Z. Recent advances in Ti-6Al-4V additively manufactured by selective laser melting for biomedical implants: Prospect development. *J. Alloys Compd.* **2022**, *896*, 163072. [[CrossRef](#)]
12. Niinomi, M. Mechanical properties of biomedical titanium alloys. *Mater. Sci. Eng. A* **1998**, *243*, 231–236. [[CrossRef](#)]
13. Wang, J.; Liu, L.; Yang, M.; Wu, X.; Li, S.; Zhang, W.; Zhang, H. Modification effect of graphene oxide on oxidation coating of Ti-3Zr-2Sn-3Mo-25 Nb near- $\beta$  titanium alloy. *J. Alloys Compd.* **2022**, *901*, 163561. [[CrossRef](#)]
14. Weng, F.; Chen, C.; Yu, H. Research status of laser cladding on titanium and its alloys: A review. *Mater. Des.* **2014**, *58*, 412–425. [[CrossRef](#)]
15. Li, G.; Zhong, X.; Wang, X.; Gong, F.; Lei, H.; Zhou, Y.; Li, C.; Xiao, Z.; Ren, G.; Zhang, L.; et al. Titanium carbide nanosheets with defect structure for photothermal-enhanced sonodynamic therapy. *Bioact. Mater.* **2022**, *8*, 409–419. [[CrossRef](#)]

16. Bordbar-Khiabani, A.; Gasik, M. Electrochemical and biological characterization of Ti–Nb–Zr–Si alloy for orthopedic applications. *Sci. Rep.* **2023**, *13*, 2312. [[CrossRef](#)] [[PubMed](#)]
17. Hao, Y.L.; Zhang, Z.B.; Li, S.J.; Yang, R. Microstructure and mechanical behavior of a Ti–24Nb–4Zr–8Sn alloy processed by warm swaging and warm rolling. *Acta Mater.* **2012**, *60*, 2169–2177. [[CrossRef](#)]
18. Fer, B.; Tingaud, D.; Hocini, A.; Hao, Y.; Leroy, E.; Prima, F.; Dirras, G. Powder Metallurgy Processing and Mechanical Properties of Controlled Ti-24Nb-4Zr-8Sn Heterogeneous Microstructures. *Metals* **2020**, *10*, 1626. [[CrossRef](#)]
19. Zhang, Y.W.; Li, S.J.; Obbard, E.G.; Wang, H.; Wang, S.C.; Hao, Y.L.; Yang, R. Elastic properties of Ti–24Nb–4Zr–8Sn single crystals with bcc crystal structure. *Acta Mater.* **2011**, *59*, 3081–3090. [[CrossRef](#)]
20. Nune, K.C.; Misra, R.D.K.; Li, S.J.; Hao, Y.L.; Yang, R. Osteoblast cellular activity on low elastic modulus Ti–24Nb–4Zr–8Sn alloy. *Dent. Mater.* **2017**, *33*, 152–165. [[CrossRef](#)]
21. Li, X.; Wang, J.; Ye, S.; Zhou, Y.; Yu, P. An investigation of the tensile deformation mechanism of a high-oxygen Ti2448 alloy fabricated by powder metallurgy by use of the in-situ EBSD method. *Mater. Sci. Eng. A* **2021**, *828*, 141981. [[CrossRef](#)]
22. Tang, Z.; Wei, X.; Li, T.; Wu, H.; Xiao, X.; Hao, Y.; Li, S.; Hou, W.; Shi, L.; Li, X.; et al. Three-Dimensionally Printed Ti2448 with Low Stiffness Enhanced Angiogenesis and Osteogenesis by Regulating Macrophage Polarization via Piezo1/YAP Signaling Axis. *Front. Cell Dev. Biol.* **2021**, *9*, 750948. [[CrossRef](#)] [[PubMed](#)]
23. Madonsela, J.; Matizanhuka, W.; Machaka, R.; Shongwe, B.; Yamamoto, A. Sintering Performance and Corrosion behavior of biomedical Ti-24Nb-4Zr-8Sn alloy produced using SPS in various simulated body solutions. *IOP Conf. Ser. Mater. Sci. Eng.* **2018**, *430*, 012037. [[CrossRef](#)]
24. Zhang, Y.; Wang, J.; Wang, P.; Fan, X.; Li, X.; Fu, J.; Li, S.; Fan, H.; Guo, Z. Low elastic modulus contributes to the osteointegration of titanium alloy plug. *J. Biomed. Mater. Res. Part A* **2013**, *101B*, 584–590. [[CrossRef](#)] [[PubMed](#)]
25. Liu, C.-F.; Li, S.-J.; Hou, W.-T.; Hao, Y.-L.; Huang, H.-H. Enhancing corrosion resistance and biocompatibility of interconnected porous  $\beta$ -type Ti-24Nb-4Zr-8Sn alloy scaffold through alkaline treatment and type I collagen immobilization. *Appl. Surf. Sci.* **2019**, *476*, 325–334. [[CrossRef](#)]
26. Xu, R.; Tan, Z.; Xiong, D.; Fan, G.; Guo, Q.; Zhang, J.; Su, Y.; Li, Z.; Zhang, D. Balanced strength and ductility in CNT/Al composites achieved by flake powder metallurgy via shift-speed ball milling. *Compos. Part A Appl. Sci. Manuf.* **2017**, *96*, 57–66. [[CrossRef](#)]
27. Chiba, A.; Daino, Y.; Aoyagi, K.; Yamanaka, K. Smoke Suppression in Electron Beam Melting of Inconel 718 Alloy Powder Based on Insulator–Metal Transition of Surface Oxide Film by Mechanical Stimulation. *Materials* **2021**, *14*, 4662. [[CrossRef](#)]
28. Yim, S.; Aoyagi, K.; Yanagihara, K.; Bian, H.; Chiba, A. Effect of mechanical ball milling on the electrical and powder bed properties of gas-atomized Ti–48Al–2Cr–2Nb and elucidation of the smoke mechanism in the powder bed fusion electron beam melting process. *J. Mater. Sci. Technol.* **2023**, *137*, 36–55. [[CrossRef](#)]
29. Salur, E.; Aslan, A.; Kuntoğlu, M.; Acarer, M. Effect of ball milling time on the structural characteristics and mechanical properties of nano-sized  $Y_2O_3$  particle reinforced aluminum matrix composites produced by powder metallurgy route. *Adv. Powder Technol.* **2021**, *32*, 3826–3844. [[CrossRef](#)]
30. Pradeep, N.B.; Hegde, M.M.R.; Patel, G.C.M.; Giasin, K.; Pimenov, D.Y.; Wojciechowski, S. Synthesis and characterization of mechanically alloyed nanostructured ternary titanium based alloy for biomedical applications. *J. Mater. Res. Technol.* **2022**, *16*, 88–101. [[CrossRef](#)]
31. Li, X.; Ye, S.; Yuan, X.; Yu, P. Fabrication of biomedical Ti-24Nb-4Zr-8Sn alloy with high strength and low elastic modulus by powder metallurgy. *J. Alloy. Compd.* **2019**, *772*, 968–977. [[CrossRef](#)]
32. Yang, C.L.; Zhang, Z.J.; Li, S.J.; Liu, Y.J.; Sercombe, T.B.; Hou, W.T.; Zhang, P.; Zhu, Y.K.; Hao, Y.L.; Zhang, Z.F.; et al. Simultaneous improvement in strength and plasticity of Ti-24Nb-4Zr-8Sn manufactured by selective laser melting. *Mater. Des.* **2018**, *157*, 52–59. [[CrossRef](#)]
33. Sames, W.J.; List, F.A.; Pannala, S.; Dehoff, R.R.; Babu, S.S. The metallurgy and processing science of metal additive manufacturing. *Int. Mater. Rev.* **2016**, *61*, 315–360. [[CrossRef](#)]
34. Sun, F.J.; Qu, S.G.; Deng, Z.H.; Su, F.; Li, X.Q. Shear band formation and wear mechanism of titanium alloy powder metallurgy material prepared by HIP using Ti-6Al-4V pre-alloy powder. *Int. J. Adv. Manuf. Technol.* **2017**, *93*, 4439–4445. [[CrossRef](#)]
35. Jiang, X.; Bai, J.; Yang, N.; Ran, Q.; Wang, S. Effect of deformation on  $\alpha$ - $\beta$  phase transformation temperature of a metastable TiZr based alloy. *Mater. Lett.* **2021**, *285*, 129003. [[CrossRef](#)]
36. Kumar, K.N.; Muneshwar, P.; Singh, S.K.; Jha, A.K.; Pant, B.; George, K.M. Effect of Grain Boundary Alpha on Mechanical Properties of  $Ti_{5.4}Al_3Mo_1V$  Alloy. *JOM* **2015**, *67*, 1265–1272. [[CrossRef](#)]
37. Banerjee, R.; Bhattacharyya, D.; Collins, P.C.; Viswanathan, G.B.; Fraser, H.L. Precipitation of grain boundary  $\alpha$  in a laser deposited compositionally graded Ti–8Al–xV alloy—An orientation microscopy study. *Acta Mater.* **2004**, *52*, 377–385. [[CrossRef](#)]
38. Sen, I.; Tamirisakandala, S.; Miracle, D.B.; Ramamurty, U. Microstructural effects on the mechanical behavior of B-modified Ti–6Al–4V alloys. *Acta Mater.* **2007**, *55*, 4983–4993. [[CrossRef](#)]
39. Shi, R.; Dixit, V.; Viswanathan, G.B.; Fraser, H.L.; Wang, Y. Experimental assessment of variant selection rules for grain boundary  $\alpha$  in titanium alloys. *Acta Mater.* **2016**, *102*, 197–211. [[CrossRef](#)]
40. Hariharan, A.; Goldberg, P.; Gustmann, T.; Maawad, E.; Pilz, S.; Schell, F.; Kunze, T.; Zwahr, C.; Gebert, A. Designing the microstructural constituents of an additively manufactured near  $\beta$  Ti alloy for an enhanced mechanical and corrosion response. *Mater. Des.* **2022**, *217*, 110618. [[CrossRef](#)]

41. Yang, J.; Yu, H.; Yin, J.; Gao, M.; Wang, Z.; Zeng, X. Formation and control of martensite in Ti-6Al-4V alloy produced by selective laser melting. *Mater. Des.* **2016**, *108*, 308–318. [[CrossRef](#)]
42. Kumar, P.; Ramamurty, U. Microstructural optimization through heat treatment for enhancing the fracture toughness and fatigue crack growth resistance of selective laser melted Ti 6Al 4V alloy. *Acta Mater.* **2019**, *169*, 45–59. [[CrossRef](#)]
43. Xue, A.; Lin, X.; Wang, L.; Wang, J.; Huang, W. Influence of trace boron addition on microstructure, tensile properties and their anisotropy of Ti6Al4V fabricated by laser directed energy deposition. *Mater. Des.* **2019**, *181*, 107943. [[CrossRef](#)]
44. Foltz, J.W.; Welk, B.; Collins, P.; Fraser, H.L.; Williams, J.C. Formation of Grain Boundary  $\alpha$  in  $\beta$  Ti Alloys: Its Role in Deformation and Fracture Behavior of These Alloys. *Met. Mater. Trans. A* **2011**, *42*, 645–650. [[CrossRef](#)]
45. Bermingham, M.; McDonald, S.; Dargusch, M. Effect of trace lanthanum hexaboride and boron additions on microstructure, tensile properties and anisotropy of Ti-6Al-4V produced by additive manufacturing. *Mater. Sci. Eng. A* **2018**, *719*, 1–11. [[CrossRef](#)]
46. Zhang, K.; Tian, X.; Bermingham, M.; Rao, J.; Jia, Q.; Zhu, Y.; Wu, X.; Cao, S.; Huang, A. Effects of boron addition on microstructures and mechanical properties of Ti-6Al-4V manufactured by direct laser deposition. *Mater. Des.* **2019**, *184*, 108191. [[CrossRef](#)]
47. Liu, C.M.; Wang, H.M.; Tian, X.J.; Liu, D. Development of a pre-heat treatment for obtaining discontinuous grain bound-ary  $\alpha$  in laser melting deposited Ti-5Al-5Mo-5V-1Cr-1Fe alloy. *Mater. Sci. Eng. A* **2014**, *604*, 176–182. [[CrossRef](#)]

**Disclaimer/Publisher’s Note:** The statements, opinions and data contained in all publications are solely those of the individual author(s) and contributor(s) and not of MDPI and/or the editor(s). MDPI and/or the editor(s) disclaim responsibility for any injury to people or property resulting from any ideas, methods, instructions or products referred to in the content.